

Supporting Information

Designed synthesis of NiCo-LDH and derived sulfide on heteroatoms
doping edge-enriched 3D rivet graphene films for high-performance
asymmetric supercapacitor and efficient OER

Kaiqiang Qin^a, Liping Wang^a, Shuaiwei Wen^a, Lechen Diao^a, Peng Liu^a, Jiajun Li^a, Liying
Ma^a, Chunsheng Shi^a, Cheng Zhong^a, Wenbin Hu^a, Enzuo Liu^{a,b,*} and Naiqin Zhao^{a,b*}

^a School of Materials Science and Engineering and Tianjin Key Laboratory of Composites
and Functional Materials, Tianjin University, Tianjin 300072, China.

^b Collaborative Innovation Center of Chemical Science and Engineering, Tianjin, 300072,
China

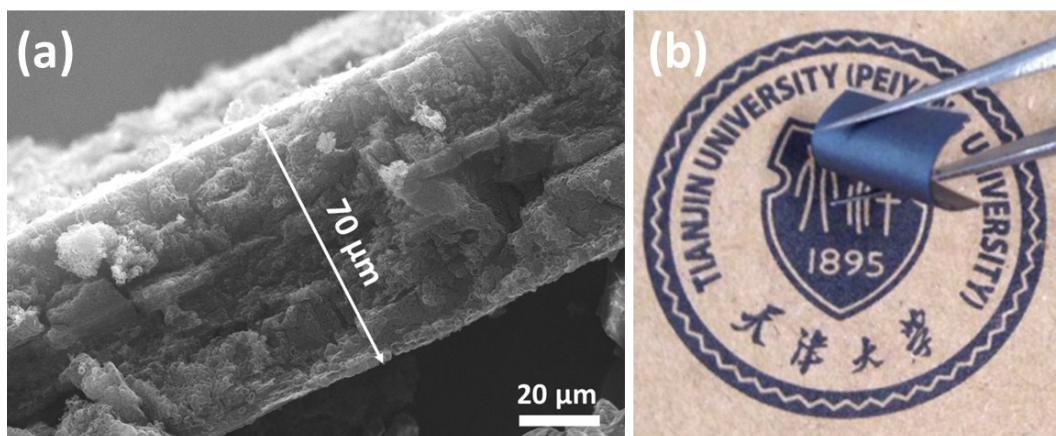


Fig. S1 (a) The cross-sectional SEM image of H-3DRG film. (b) The photograph of the free-standing flexible H-3DRG film.

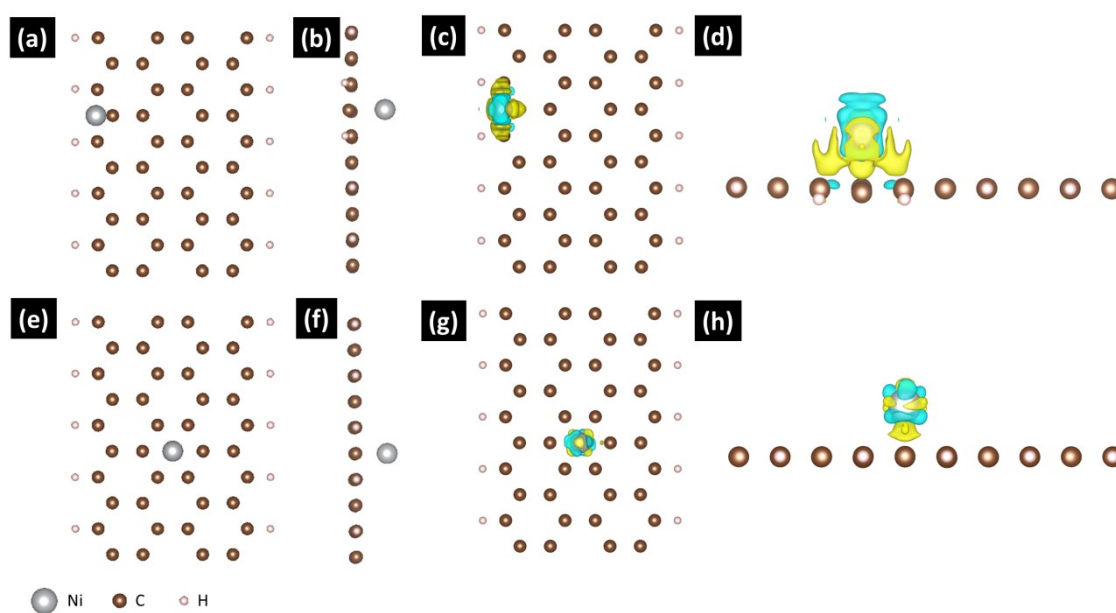


Fig. S2 (a) Top and (b) side views of Ni atom adsorbing nearby the carbon atoms located at the edge of the graphene. (c) Top and (d) side views of charge density difference of C/Ni interface located at the edge of the graphene. (e) Top and (f) side views of Ni atom adsorbing at the center of the graphene. (g) Top and (h) side views of charge density difference of C/Ni interface located at the center of the graphene. The smallest balls represent H atoms used to saturate the dangling bonds of carbon atoms at the edge.

In order to get a better picture of weak interactions,^{S1} we choose a computationally cost-effective “optB88-vdW” method for vdW interactions.^{S2} The exchange-correlation functional is approximated with the local density approximation.^{S3} The Gaussian smearing method^{S4} was used, and the width of smearing was chosen as 0.05 eV. The energy cutoff for plane-wave expansion of the PAW’s is 400 eV. The optimized lattice constants of graphene is 2.45Å, consistent with the experimental results (2.46 Å).^{S5} The supercell of the graphene nanosheet contains 40 C atoms. In the vertical direction, a vacuum layer of about 20 Å in thickness is introduced for all the surfaces and interfaces. The Brillouin zone^{S6} is sampled using Monkhorst-Pack scheme with a k-point mesh of 3×3×1 in the Gamma-centered grids for the structural relaxation, and 5×5×1 k-point mesh is used for the static calculations of all the systems. The structure relaxation is continued until the forces on all the atoms are converged to less than 0.01 eV/Å. Fig. S2c, d, g and h are the charge density differences of the stable configurations with one Ni atom adsorbed on the central and edge of graphene, respectively, which are obtained by subtracting the charge density of the isolated graphene and the isolated Ni atom from that of the graphene with one Ni atom adsorbed. The isosurface value is set to 0.009 e/Å³. Light blue and yellow represent charge loss and accumulation, respectively.

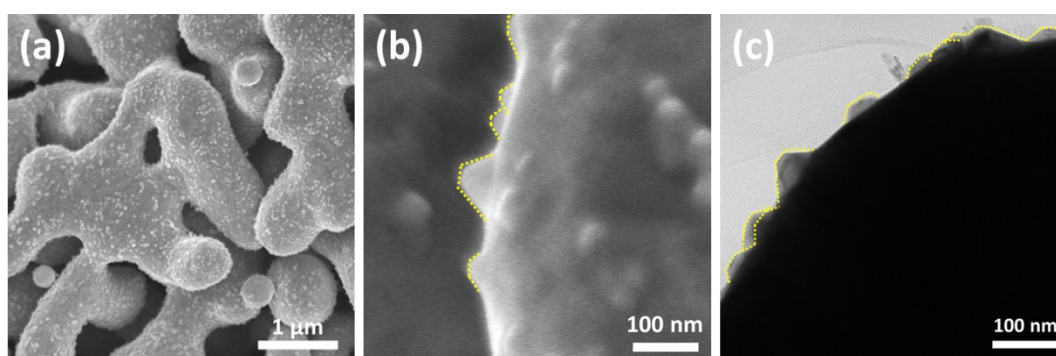


Fig. S3 (a, b) The SEM images with different magnification and (c) TEM image of NPC after annealed for 1 min at 900 °C under Ar and H₂.

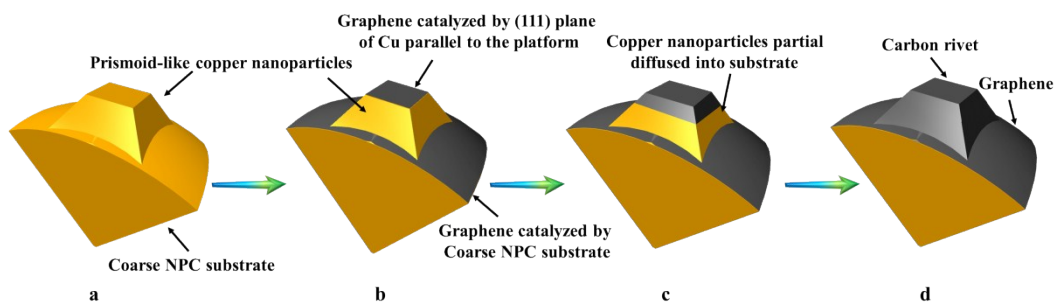


Fig. S4 Schematic illustrations of the formation process of 3D rivet graphene.

Firstly, large amount of prismatic-like copper nanoparticles remain on the surface of coarse NPC substrates after annealing for 1 min at 900 °C under Ar and H₂ (Fig. S4a). Subsequently, a thin layer of edge-enriched graphene film was grown onto the surface of (111) plane of Cu nanoparticle parallel to the platform under the mixed atmosphere of C₂H₂, NH₃, Ar and H₂ (Fig. S4b). Meanwhile, the copper nanoparticles diffused into the coarse NPC substrate gradually at high temperature and still have the catalysis ability for the fabrication of graphene (Fig. S4c). The thickness of the graphene layer catalyzed by copper nanoparticles increased gradually along with the diffusion process and formed the edge-enriched 3D rivet graphene (3DRG) structure (Fig. S4d).

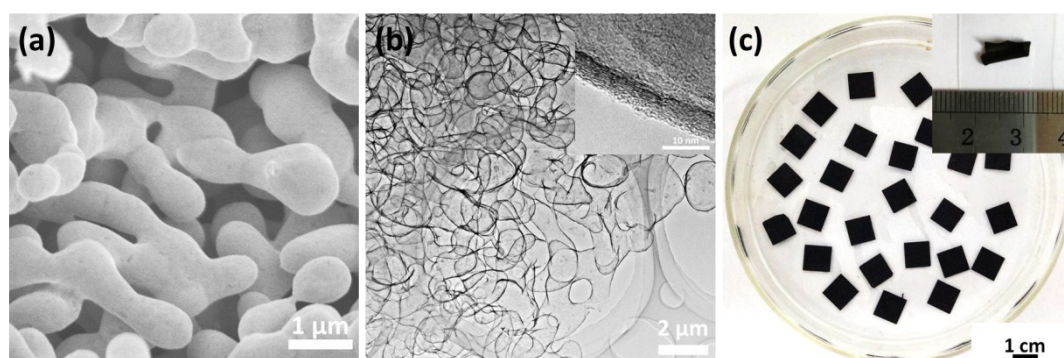


Fig. S5 (a) The SEM image of NPC after annealed for 3 min at 900 °C. (b) TEM images of H-3DG. The inset shows the high-magnification TEM of H-3DG. (c) The photograph of the free-standing H-3DG film in water. The inset shows the broken and coiled H-3DG film after traditional heat-dry approach.

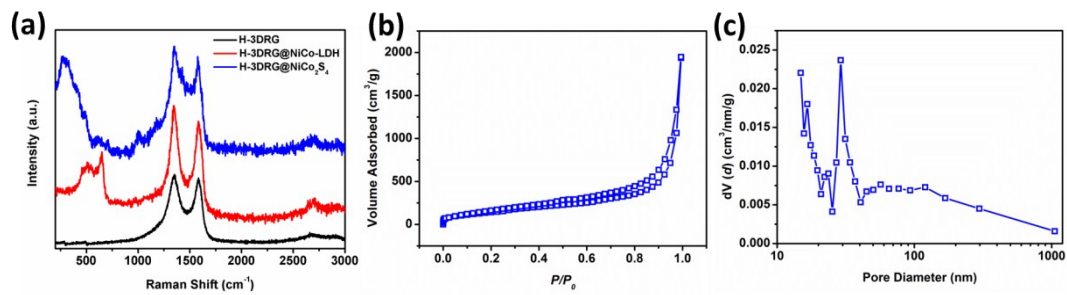


Fig. S6 (a) Raman analysis of the H-3DRG, H-3DRG@NiCo-LDH and H-3DRG@NiCo₂S₄ films. (b) Nitrogen adsorption-desorption isotherm of H-3DRG films. (c) BJH pore size distribution of H-3DRG films.

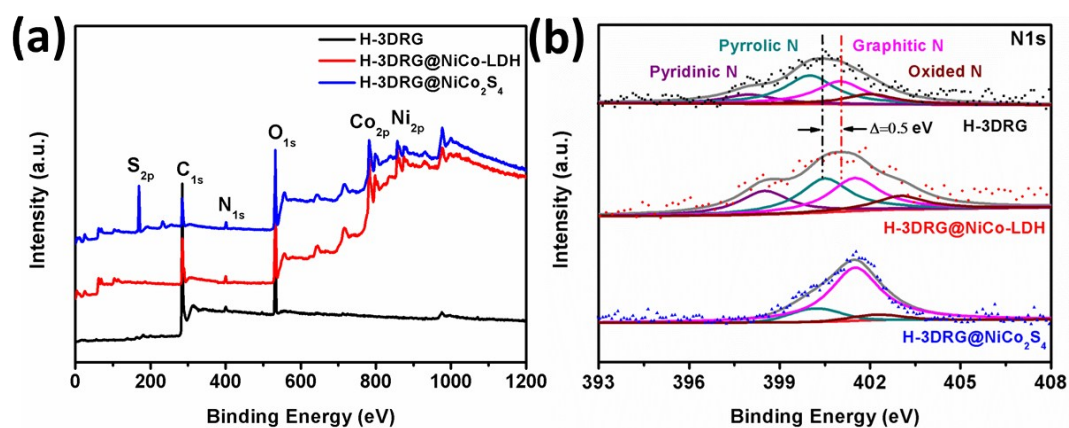


Fig. S7 (a) XPS spectra of the surface chemical composition of as-prepared H-3DRG, H-3DRG@NiCo-LDH and H-3DRG@NiCo₂S₄ films. (b) The comparison of N_{1s} XPS spectrum of H-3DRG, H-3DRG@NiCo-LDH and H-3DRG@NiCo₂S₄ hybrids.

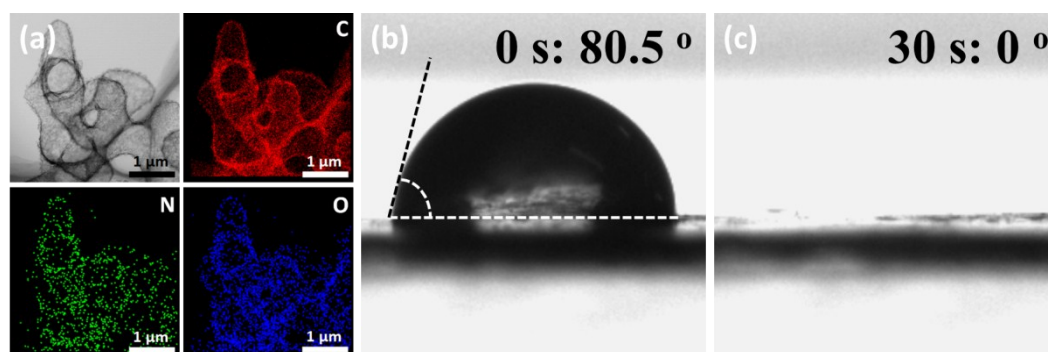


Fig. S8 (a) STEM image and corresponding elemental mapping images of C, N and O. (b) Dynamic contact angle measurements for H-3DRG film.

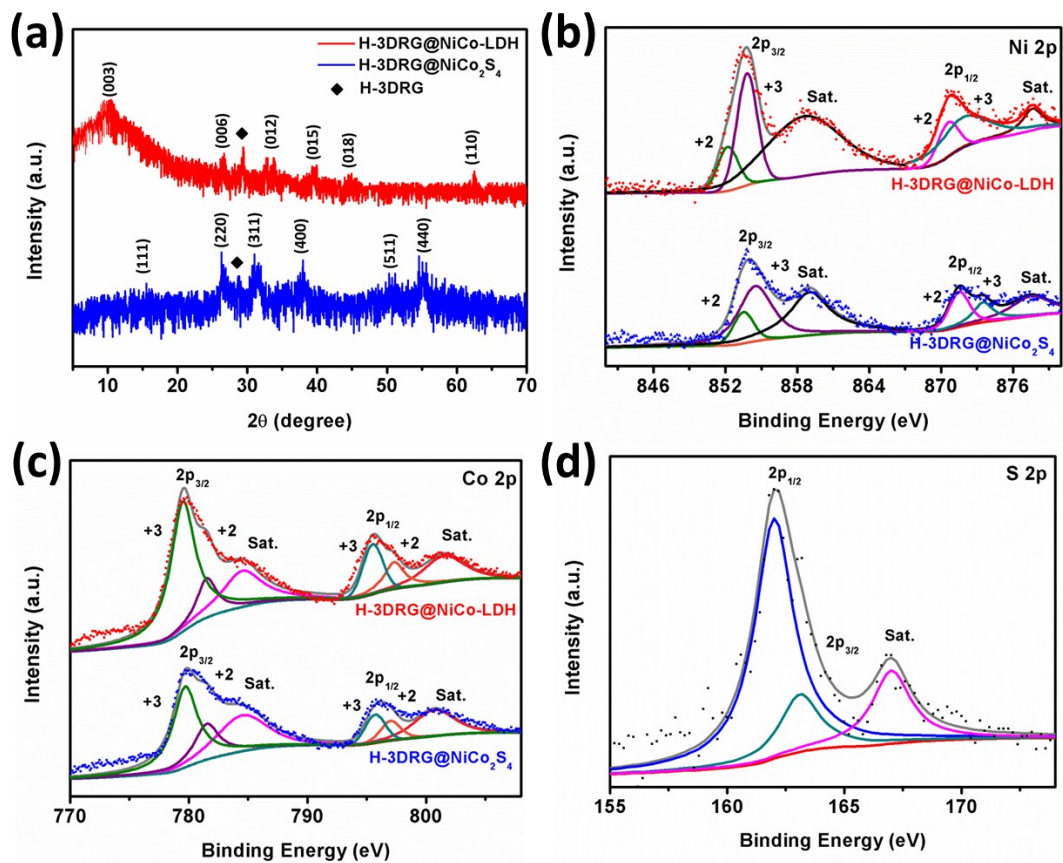


Fig. S9 (a) The XRD patterns of the as-prepared H-3DRG@NiCo-LDH and H-3DRG@NiCo₂S₄ hybrid films. (b) The Ni 2p XPS spectrum of the as-prepared H-3DRG@NiCo-LDH and H-3DRG@NiCo₂S₄ hybrid films. (c) The Co 2p XPS spectrum of the as-prepared H-3DRG@NiCo-LDH and H-3DRG@NiCo₂S₄ hybrid films. (d) The S 2p XPS spectrum of the as-prepared H-3DRG@NiCo₂S₄ hybrid films.

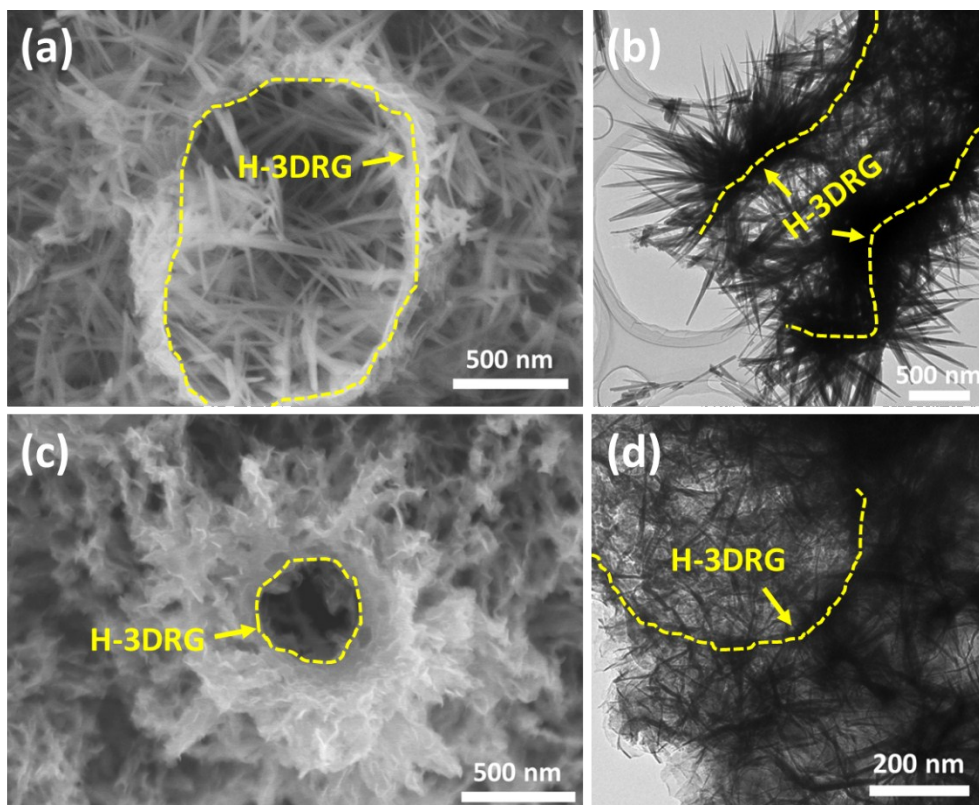


Fig. S10 (a) The SEM and (b) TEM images of NiCo-LDH nanoneedles grown onto the inner and outer sides of H-3DRG film after hydrothermal for 15 h. (c) The SEM and (d) TEM images of NiCo₂S₄ nanostructure grown onto the inner and outer sides of H-3DRG film after anion exchange process.

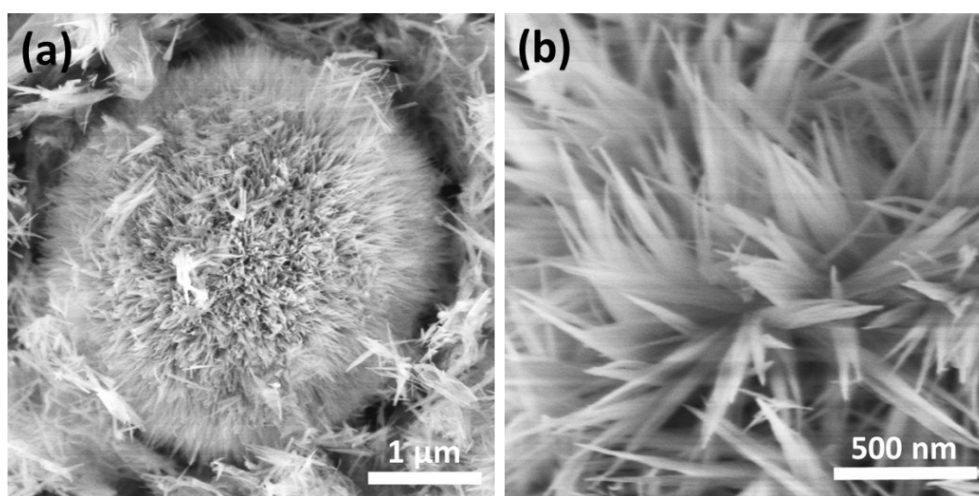


Fig. S11 The SEM images of pristine NiCo-LDH sample fabricated without H-3DRG films.

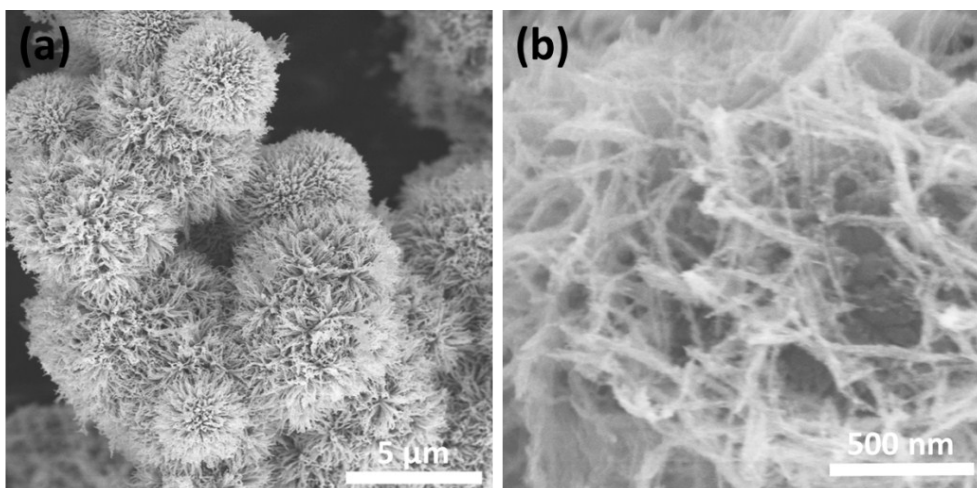


Fig. S12 The SEM images of pristine NiCo_2S_4 sample fabricated without H-3DRG films.

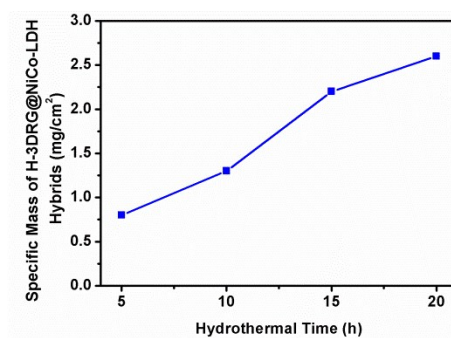


Fig. S13 The total specific mass of H-3DRG@NiCo-LDH hybrids with different hydrothermal time.

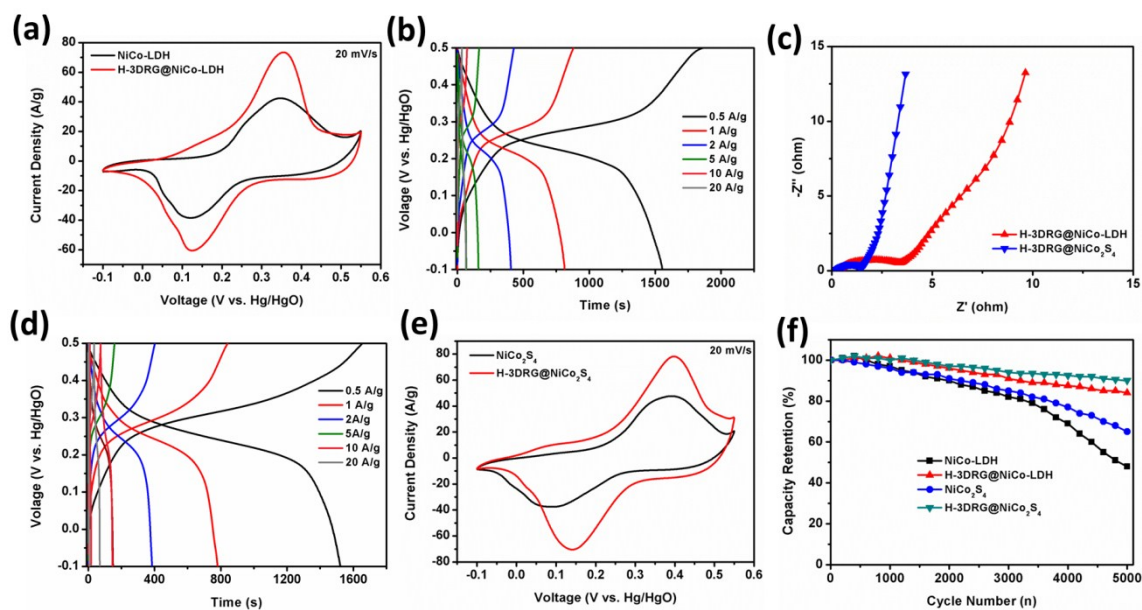


Fig. S14 (a) CV curves of the H-3DRG@NiCo-LDH and pristine NiCo-LDH electrodes at a scan rate of 20 mV/s. (b) GCD curves of the H-3DRG@NiCo-LDH hybrid electrode at different densities from 0.5 to 20 A/g. (c) Nyquist plot of H-3DRG@NiCo-LDH and H-3DRG@NiCo₂S₄ hybrid electrodes, respectively. (d) GCD curves of the H-3DRG@NiCo₂S₄ hybrid electrode at different densities from 0.5 to 20 A/g. (e) CV curves of the H-3DRG@NiCo₂S₄ and pristine NiCo₂S₄ electrodes at a scan rate of 20 mV/s. (f) Cycling performance of the pristine NiCo-LDH, NiCo₂S₄, H-3DRG@NiCo-LDH and H-3DRG@NiCo₂S₄ hybrid electrodes at a current density of 10 A/g.

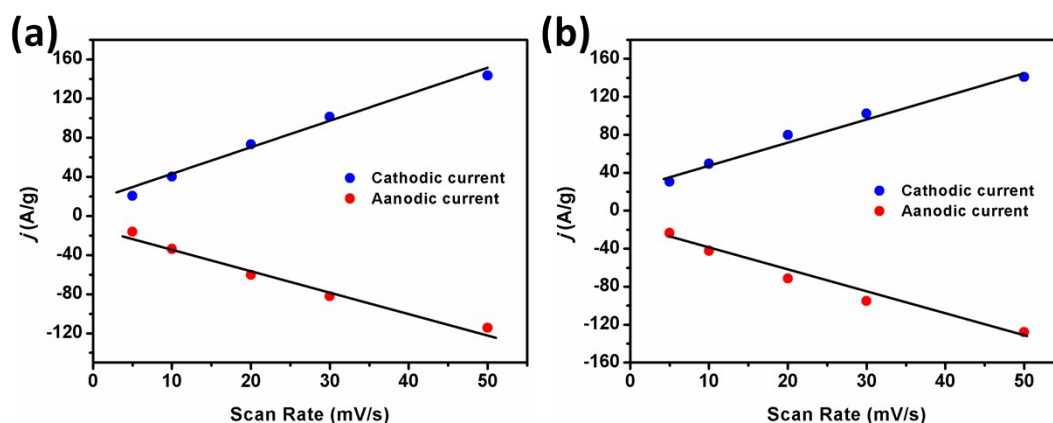


Figure S15. Correlation between the peak current and scan rate for the redox of (a) H-3DRG@NiCo-LDH and (b) H-3DRG@NiCo₂S₄ hybrids.

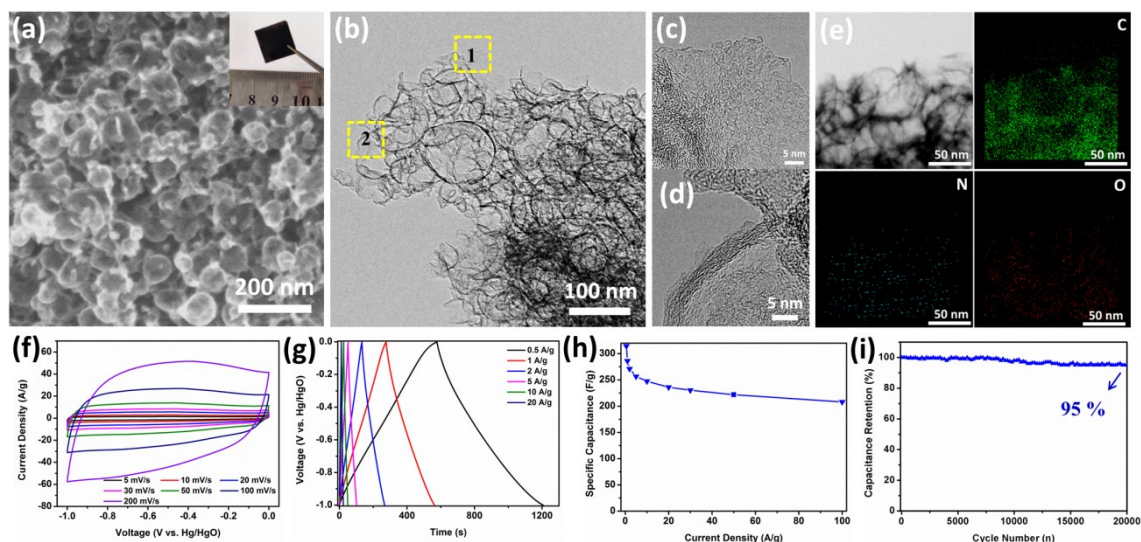


Fig. S16 (a) SEM image of NO-3DnpG after removing the NPC substrate (inset: photograph of the free-standing NO-3DnpG film). (b) TEM image of NO-3DnpG. (c) and (d) High-resolution TEM (HRTEM) images of NO-3DnpG of the area 1 and 2 in (b), respectively. (e) STEM image and corresponding elemental mapping images of C, N and O. (f) CV curves of single NO-3DnpG electrode collected at different scan rates in 6 M KOH electrolyte. (g) Galvanostatic charge/discharge curves at various current densities. (h) The specific capacitance of the NO-3DnpG electrode at different current densities. (i) Long-term charge/discharge cycling performance of the flexible NO-3DnpG electrode.

The HG was fabricated by low-temperature CVD approach using NPC as the catalyst and substrate, which has been reported in our previous work.^{S7} After annealed for a short time at 800 °C, the NPC substrate was coarsened to a particle-linked architecture with a ligament size of 40 - 100 nm. HG layer coated onto the surface of NPC was carbonized, and the NO-3DnpG maintained a free-standing nanoporous film with pore size of 40 - 100 nm and thickness of 100 μm (Fig. S15a). TEM images reveal that the HG layer was converted into 3D nanoporous graphene less than 10 layers and presents large amount of micropores on the surface of graphene caused by nitrogen doping (Fig. S15b-d). Furthermore, the elemental mapping

confirms that the graphene is doped with nitrogen and oxygen elements successfully (Fig. S15e).

The flexible NO-3DnpG can be directly used as binder-free working electrode, which was tested in a three-electrode cell in 6 M KOH electrolyte. The ideal rectangular shapes of CV curves and symmetric GCD curves suggest that the NO-3DnpG electrode shows an ideal supercapacitance behavior (Fig. S15f and g). Moreover, the NO-3DnpG electrode can achieve a high specific capacitance of 310 F/g at 1 A/g and still remain 220 F/g at 100 A/g (Fig. S15h). More importantly, a high cycle stability of 95 % retention is achieved after 20000 cycling, which indicates the NO-3DnpG film is an ideal negative electrode for ASCs (Fig. S15i).

For the asymmetric supercapacitor, the mass balance is determined as follows.

$$m_c C_{S_c} V_c = m_b Q_b \quad (1)$$

$$m_c / m_b = Q_b / C_{S_c} / V_c \quad (2)$$

where m_c is the mass of the capacitor or pseudocapacitive electrode, C_{S_c} is the specific capacitance of the capacitor or pseudocapacitive electrode, V_c is the potential window of the capacitor or pseudocapacitive electrode, m_b is the mass of the battery-type electrode and Q_b is the capacity of the battery-type electrode.

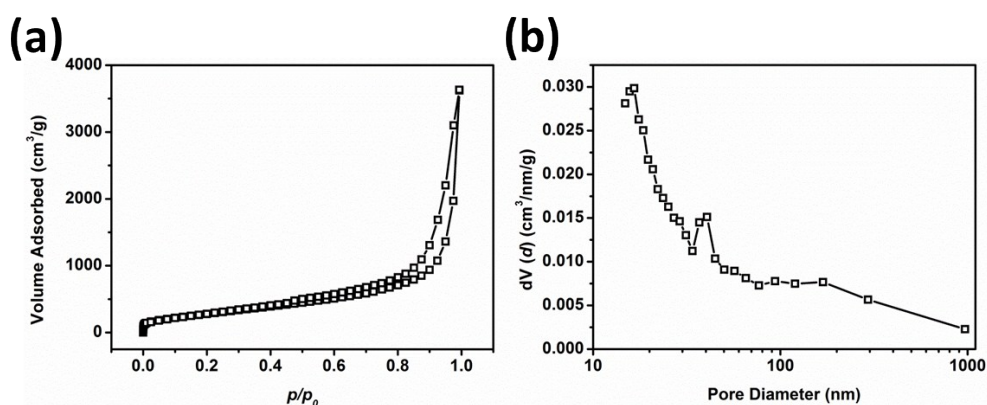


Fig. S17 (a) Nitrogen adsorption-desorption isotherm of NO-3DnpG. (b) BJH pore size distribution of NO-3DnpG.

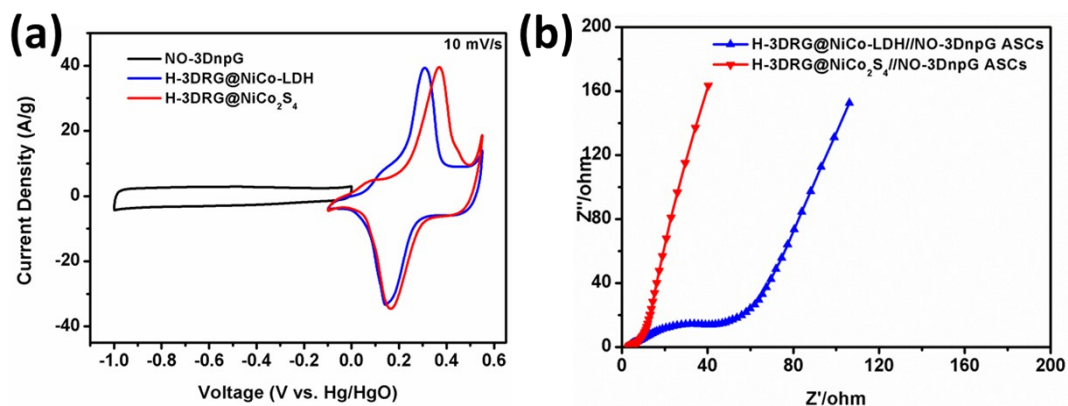


Fig. S18 (a) CV curves of the NO-3DnpG, H-3DRG@NiCo-LDH and H-3DRG@NiCo₂S₄ hybrids electrodes at a constant scan rate of 10 mV/s. (b) Nyquist plots of electrochemical impedance spectroscopy (EIS) data for the H-3DRG@NiCo-LDH//NO-3DnpG ASCs and H-3DRG@NiCo₂S₄//NO-3DnpG ASCs.

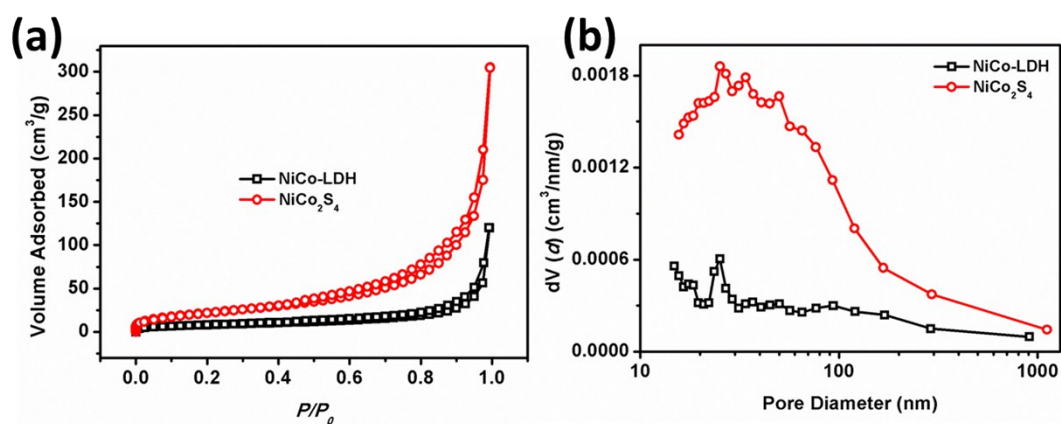


Fig. S19 (a) Nitrogen adsorption-desorption isotherm and (b) BJH pore size distribution of NiCo-LDH and NiCo₂S₄.

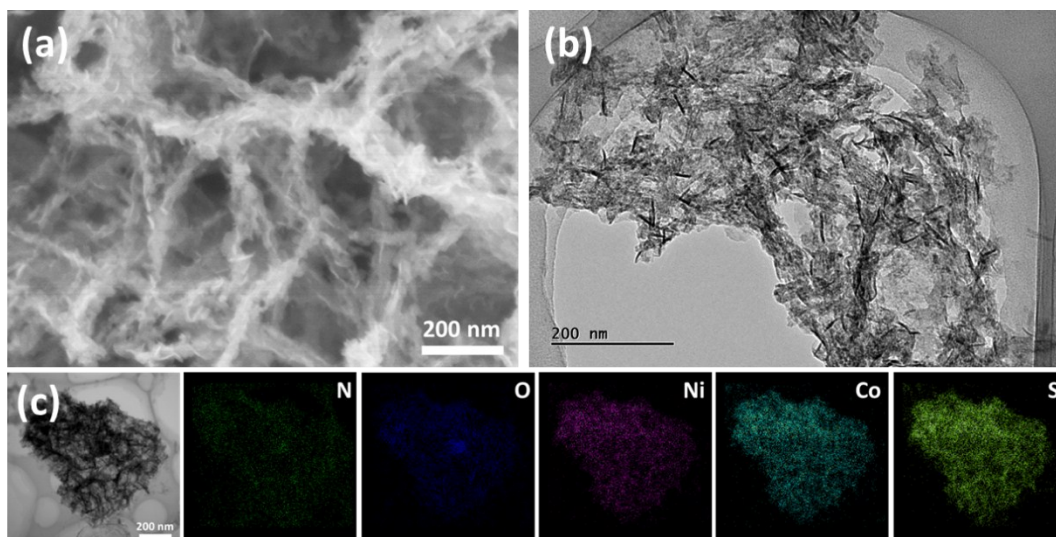


Fig. S20 (a) SEM, (b) TEM and (c) elemental mapping images of H-3DRG@NiCo₂S₄ electrode after long-term OER electrolysis.

Reference

- [S1] A. Tkatchenko, R. Car, M. Scheffler, *Phys. Rev. Lett.* 108 (2012) 236402.
- [S2] E. Hzarati, G. Wijs, G. Brocks, *Phys. Rev. B* 90 (2014) 155448.
- [S3] T. Björkman, A. Gulans, A. Krasheninnikov, R. Nieminen, *J. Phys.: Condens. Matter* 24 (2012) 424218.
- [S4] M. Methfessel, A. Paxton, *Phys. Rev. B* 40 (1989) 3616.
- [S5] Y. Baskin, L. Meyer, *Phys. Rev.* 100 (1955) 544-544.
- [S6] S. Froyen, *Phys. Rev. B: Condens. Matter* 39 (1989) 3168.
- [S7] K. Qin, J. Kang, J. Li, E. Liu, C. Shi, Z. Zhang, X. Zhang, N. Zhao, *Nano Energy* 24 (2016) 158-164.